



Facile assembly of $\text{Bi}_2\text{O}_3/\text{Bi}_2\text{S}_3/\text{MoS}_2$ *n-p* heterojunction with layered $n\text{-}\text{Bi}_2\text{O}_3$ and $p\text{-}\text{MoS}_2$ for enhanced photocatalytic water oxidation and pollutant degradation

Jun Ke^{a,b}, Jie Liu^a, Hongqi Sun^a, Huayang Zhang^a, Xiaoguang Duan^a, Ping Liang^a, Xinyong Li^a, Moses O. Tade^a, Shaomin Liu^a, Shaobin Wang^{a,*}

^a Department of Chemical Engineering, Curtin University, Perth, GPO Box U1987, WA 6845, Australia

^b School of Chemistry and Environmental Engineering, Wuhan Institute of Technology, Wuhan 430073, China



ARTICLE INFO

Article history:

Received 17 May 2016

Received in revised form 22 June 2016

Accepted 28 June 2016

Available online 28 June 2016

Keywords:

Photocatalysis

p-n Heterojunction

Bismuth trioxide

MoS_2

O_2 evolution

ABSTRACT

As an important half reaction in solar-driven water splitting, it is still a challenging issue to develop low-cost and high efficient photocatalysts for water oxidation process. In this study, we reported a facile strategy for controllable synthesis of three-component $\text{Bi}_2\text{O}_3/\text{Bi}_2\text{S}_3/\text{MoS}_2$ *n-p* heterojunction based on the formation of the intermediate Bi_2S_3 by coupling Bi_2O_3 and MoS_2 . The Bi_2S_3 was easily formed due to the strong interaction between Bi^{3+} and S^{2-} ions with the assistance of the hydrothermal treatment. As a result, the prepared $\text{Bi}_2\text{O}_3/\text{Bi}_2\text{S}_3/\text{MoS}_2$ nanocomposite exhibits enhanced ability of photocatalytic water oxidation ($529.1 \mu\text{mol h}^{-1} \text{g}^{-1}$ cat), which is 1.5 and 12.5 times higher than that of pure Bi_2O_3 and MoS_2 , respectively, under simulated solar light irradiation. Furthermore, the photoelectrochemical results reveal that the charge transportation feature and the donor density were apparently enhanced after the introduction of highly conductive layered MoS_2 , which indicates the enhancement of the photo-response and the improvement of charge separation efficiency.

© 2016 Elsevier B.V. All rights reserved.

1. Introduction

Energy crisis triggers the rapid development of promising and inexpensive methods for clean energy production, such as photocatalytic water splitting [1,2]. It is well-known that the photocatalytic water splitting process includes hydrogen evolution reaction and oxygen evolution reaction. In general, oxygen evolution reaction is multi-electrons transfer reaction, which is a sluggish process and involves complicated breaking of $\text{O}-\text{H}$ bond and formation of $\text{O}-\text{O}$ bond [3]. Currently, most of efficient water oxidation catalysts (WOCs) consist of noble metals Ru and Ir, however, the scarcity and high cost hinder their widespread application [4–6]. In order to reduce the cost, some transition metals are utilized to synthesize promising WOCs due to their less expense, earth-abundance, and low toxicity [7–9]. Bismuth trioxide (Bi_2O_3) stands out among many attractive candidate materials because of its low cost, favorable direct band gap of 2.5–2.8 eV, and good photostability in acidic conditions [10,11]. The valence band edge of Bi_2O_3

(+3.13 V vs NHE) is enough positive to provide sufficient potential for oxygen production. In addition, Bi_2O_3 is one of semiconductors with multiple crystal structures, possessing either *n*-type or *p*-type properties [12] and allowing it to be easily used in sensor, catalysis, and photovoltaic field [13–15]. Nevertheless, as similar to many semiconductors, the poor harvesting of solar energy and charge carrier separation of pure Bi_2O_3 leads to the low photocatalytic activity and thus cannot meet the demand of commercial applications.

On the other hand, in contrast to single component photocatalysts, heterojunction photocatalysts that combine at least two disparate functional materials in one system have received more attention in the past decades [16–18]. Among advanced heterojunction materials, *p-n* heterojunctions are extensively studied and reported, which simultaneously realize high utilization of solar energy and efficiency of photoinduced charge separation by means of formation of an inner electric field between the *n*-type and *p*-type semiconductors [19]. Therefore, to improve the photocatalytic performance of Bi_2O_3 , it is necessary to couple Bi_2O_3 with other semiconductors for constructing a heterojunction system. Among numerous semiconductors, molybdenum disulphide (MoS_2), as a graphene-like transition metal dichalcogenide, may be a good candidate for tuning photo-response and improving charge carrier transportation properties [20–23]. In fact, MoS_2 is often used

* Corresponding author.

E-mail addresses: shaobin.wang@curtin.edu.au, shaobin.wang@exchange.curtin.edu.au (S. Wang).

as an effective cocatalyst in the photocatalytic or electrocatalytic hydrogen evolution reaction due to its large surface area and high electrical conductivity [20,24–26]. These studies reveal that the incorporation of layered MoS₂ with a metal oxide can promote the photocatalytic activity.

Based on the above strategy, herein, by means of coupling Bi₂O₃ microplates with layered MoS₂, we successfully fabricated Bi₂O₃/Bi₂S₃/MoS₂ composites to form a three-phase *p-n* heterojunction for improving efficiency of solar energy utilization and photoinduced charge transportation. The three-component *n-p* heterojunction system displays enhanced photocatalytic performance for gaseous oxygen evolution under simulated solar light irradiation. To deeply understand the charge transportation, the photoelectrochemical properties of the heterojunction system were systematically investigated. The results demonstrate that the *n-p* heterojunction system based on *n*-Bi₂O₃ and *p*-MoS₂ were successfully prepared for the first time. It is evidently observed that owing to the introduction of highly conductive layered MoS₂, the formation of Bi₂S₃ and *n-p* heterojunction is the key role in the enhancement of photocatalytic performance, which could provide deep insight into design and application of excellent photocatalysts in the future.

2. Experimental section

2.1. Materials

Bismuth nitrate pentahydrate (98.0%), sodium hydroxide (99.8%), sodium molybdite dehydrate (99.5%), thioacetamide (99.0%), 5,5-dimethyl-1-pyrroline (DMPO, >99.0%) were purchased from Sigma-Aldrich. All the chemicals were used as received without any further purification.

2.2. Synthesis of Bi₂O₃ microplates

In a typical synthesis of Bi₂O₃ microplates, 4.8 g of Bi(NO₃)₃·5H₂O was dissolved into 100 mL of deionized water, stirring for 30 min. Then the pH value of the solution was adjusted to 8.0 by using NaOH (10 M) and sonicated for 60 min. The mixed solution was stirred overnight and then precipitated. The precipitate was washed three times using absolute ethanol, purified water, and dried at 60 °C for 12 h. Finally, the light yellow precipitate was calcined at 400 °C for 2 h in air to obtain Bi₂O₃ microplates.

2.3. Synthesis of layered MoS₂

0.108 g of sodium molybdite dehydrate and 0.216 g of thioacetamide were dissolved in 36 mL of purified water, respectively. Then they were mixed, stirred for 30 min, and transferred to a 100 mL Teflon-lined autoclave. The mixture was placed at 200 °C for 24 h. A black precipitate was obtained by centrifuging, and washed using absolute ethanol and purified water. Then the precipitate was dispersed into deionized water and sonicated. The solution was transferred to a centrifugation tube and the centrifuge was set at 2000 rpm for removal of the MoS₂ aggregation at the bottom of the tube. Finally, the nanosized MoS₂ was collected by filtration using 0.22 μm filter paper, and then dried at 60 °C for 4 h.

2.4. Synthesis of Bi₂S₃

The pure Bi₂S₃ was prepared by using excess sulfur source. In a typical procedure, 0.2 g of Bi₂O₃ microplates and 0.4 g of thioacetamide were dissolved in 36 mL of purified water and stirred for 1 h. The solution was transferred to a 45 mL Teflon-lined autoclave and maintained at 200 °C for 24 h. The resulting sample was col-

lected by centrifugation, washed by deionized water, and dried in air at 60 °C for 12 h.

2.5. Synthesis of Bi₂O₃/Bi₂S₃/MoS₂ heterojunction

0.2 g of Bi₂O₃ microplates and 0.02 g of MoS₂ were added into 36 mL of absolute ethanol and stirred for 30 min. And then the mixed solution was sonicated for 30 min and transferred into a 45 mL Teflon-lined autoclave which was maintained at 140 °C for 6 h. The resulting sample was collected by centrifugation, washed by deionized water, and dried in air at 60 °C for 12 h.

2.6. Synthesis of Bi₂S₃/MoS₂ heterojunction

0.2 g of Bi₂O₃ microplates, 0.108 g of sodium molybdite dehydrate and 0.216 g of thioacetamide were dissolved in 36 mL of purified water and stirred for 1 h. The solution was transferred to a 45 mL Teflon-lined autoclave and maintained at 200 °C for 24 h. The resulting sample was collected by centrifugation, washed by deionized water, and dried in air at 60 °C for 12 h.

2.7. Characterizations

Powder X-ray diffraction (XRD) patterns of samples were determined on a Bruker D8 X-ray diffractometer (Bruker-AXS, Karlsruhe, Germany) with filtered Cu Kα radiation ($\lambda = 1.5418 \text{ \AA}$) at accelerating voltage and current of 40 kV and 40 mA, respectively. The structure and morphology of samples were observed on a field emission scanning electron microscope (FESEM, ZEISS NEON 40EsB) and transmission electron microscope (JEOL 2100). Fourier transform infrared spectra (FTIR) were recorded on a Bruker instrument with an ATR correction mode. Raman analysis was performed on an ISA dispersive Raman spectroscopy using argon ion laser with a wavelength at 514 nm. To investigate the light absorption and emission behavior, UV-vis absorption spectra were determined in diffuse reflection mode using an integrating sphere (Cary 4000). X-ray photoelectron spectroscopy (XPS) was used to determine the chemical states of elements using a Thermo Escalab 250 with Al-Kα X-ray. EPR measurements of the free radicals was recorded by using 5,5-dimethyl-1-pyrroline (DMPO, >99.0%) as a probe on a Bruker EMS-plus instrument, operated under the following conditions: center field, 3520 G; sweep width, 100 G; microwave frequency, 9.87 GHz; power setting, 18.75 mW; scan number, 3.

2.8. Photoelectrochemical measurement

Electrochemical tests were carried out using a Zahner Zennium electrochemical workstation operated in a standard three-electrode configuration with a FTO electrode deposited with the samples as a photoanode, a Pt wire as counter electrode, and Hg/Hg₂Cl₂/saturated KCl (SCE) as the reference electrode. In a typical experiment, 0.05 M Na₂SO₄ (20 mL, pH = 6.8) purged with N₂ was used as the electrolyte. For the fabrication of the photoanode, 40 mg of the solid sample was homogeneously mixed with 2 mL of absolute ethanol and 40 μL of Nafion solution (5%) by using a vortex oscillator. The obtained sample was deposited onto the as-washed FTO glass with a controlled area of 1 cm² using dip-coating to form a film electrode, and then dried in air. A 300 W Xenon lamp (Philip) coupled with an AM 1.5 G filter was applied as the simulated sunlight source ($I_0 = 100 \text{ mW cm}^{-2}$). The electrochemical impedance spectroscopy (EIS) was carried out in the frequency range of 10⁻¹–10⁵ Hz with an AC voltage amplitude of 10 mV at a DC bias of 0.298 V vs. SCE in a 0.05 M Na₂SO₄ solution.

2.9. Photocatalytic activity evaluation

In a typical procedure, photocatalytic reaction was conducted in a jacket reactor with a 300 W Xenon lamp as the simulated solar light. The photocatalytic performance was evaluated by oxidizing water molecules with AgNO_3 as an electron scavenger. More specifically, 0.1 g of catalyst samples were added to 200 mL of solution including AgNO_3 (0.03 M) and La_2O_3 (0.2 g). Before irradiation, the suspensions were mixed under vigorous stirring for 30 min in the dark and degassed for removal of O_2 in solution and air. The O_2 concentrations in the reactor were *in situ* taken by using a NEOFOX O_2 probe.

In addition, the catalyst was also tested for the degradation of methylene blue (MB). The concentrations of MB and a catalyst were 10 mg/L and 0.5 g/L, respectively, and a high-pressure Xe-lamp (300 W, Philips) was used as a simulated solar source. Prior to the illumination, the MB solution was mixed with catalysts and sonicated for 30 min in dark to establish the adsorption-desorption equilibrium. During photocatalytic degradation process, 3 mL of the reaction solution was extracted for every 15 min and measured by a UV-vis spectrophotometer (JASCOV-670).

3. Results and discussions

Pure Bi_2O_3 microplates were firstly prepared by a sol-gel method followed by calcination under 400 °C, which was utilized as a template to synthesize a pure Bi_2S_3 sample. Fig. 1a shows the crystalline phases of Bi_2O_3 and Bi_2S_3 with space groups $P2_1/c$ (JCPDS Card No.41-1449) and $Pbnm$ (JCPDS Card No.65-2435), respectively [27,28]. The strong characteristic peaks suggest the good crystallite of these samples, which indicates thioacetamide as a sulfur source successfully replaces oxygen in the lattice of Bi_2O_3 . A pure layered MoS_2 sample was synthesized through a previously reported method [29] and characterized, as shown in Fig. 1a, which displays a weak intensity of peaks due to a low degree of crystallinity. However, the XRD pattern of MoS_2 still shows identifiable characteristic peaks at 14.2°, 38.9°, 58.2° unambiguously ascribed to the (0 0 2), (1 0 3), and (1 1 0) planes of MoS_2 ($a = b = 0.316 \text{ nm}$, $c = 1.230 \text{ nm}$, JCPDS Card No.37-1492), respectively [30].

Owing to the strong affinity between Bi^{3+} ions and S^{2-} ions, they can easily bind together, resulting in formation of Bi_2S_3 crystal phase at high temperature [21,31]. It is expected that three-component heterojunction could be formed when the synthesized Bi_2O_3 and MoS_2 at a mass ratio 10 were mixed and placed at 140 °C. As a result, the XRD pattern of the composite is different from that of MoS_2 and Bi_2O_3 , which indicates formation of a new crystal phase (Fig. 1a). From the high resolution XRD patterns in Fig. 1b, we found that the strong characteristic peak at 27.7° attributed to the Bi_2O_3 (120) facet was weakened, whereas the peaks at 27.5° and 28.1° disappeared after introduction of sulfur source in Bi_2S_3 and $\text{Bi}_2\text{S}_3/\text{MoS}_2$ samples. Meanwhile, compared with the XRD pattern of pure Bi_2S_3 , it is observed that the dominant peak at 28.7° due to the Bi_2S_3 (211) facet shifts to 28.3°, which might originate from the distortion of Bi_2S_3 crystal phase. The XRD pattern of the sample denoted as $\text{Bi}_2\text{S}_3/\text{MoS}_2$ is similar to that of pure Bi_2S_3 , which indicates that excess sulfur completely replaces oxygen element in the Bi_2O_3 sample. There is no characteristic peak of MoS_2 observed in $\text{Bi}_2\text{S}_3/\text{MoS}_2$ and $\text{Bi}_2\text{O}_3/\text{Bi}_2\text{S}_3/\text{MoS}_2$ possibly due to the low content of MoS_2 in these samples. These results suggest that as combining Bi_2O_3 and MoS_2 , MoS_2 and Bi_2O_3 could act as a sulfur source and bismuth source to form Bi_2S_3 crystal phase at the contact interface.

Fig. 2 shows the morphologies of the Bi_2O_3 , Bi_2S_3 , MoS_2 , and $\text{Bi}_2\text{O}_3/\text{Bi}_2\text{S}_3/\text{MoS}_2$. The SEM image of Bi_2O_3 shows a plate-like morphology with an average 1 μm of width and 80 nm of height (Figs. 2a and S1). However, in the case of Bi_2S_3 prepared by taking advan-

tage of the Bi_2O_3 microplates as a template, the morphology of Bi_2S_3 exhibits irregular nanoparticles and nanoplates (Fig. 2b). We speculate that S^{2-} ions releasing from decomposition of thioacetamide replace O^{2-} ions, the structure of Bi_2O_3 was damaged due to the strong binding between Bi and S. Besides, the difference of unit cells between Bi_2O_3 and Bi_2S_3 results in the distortion of the nanostructures. It is observed that the layered MoS_2 nanosheets were fabricated (Fig. 2c), which is agreement with the XRD. After mixing 2D Bi_2O_3 and MoS_2 , the mixture was treated by a hydrothermal method, and consequently, we observed that these morphologies of Bi_2O_3 and MoS_2 were nicely preserved (Fig. 2d). The three-component composites have been investigated by a transmission electron microscope (TEM), as shown in Fig. 3. The low magnification TEM displays bright and dark areas due to the different thickness between Bi_2O_3 and MoS_2 , which demonstrates the coupling of Bi_2O_3 and MoS_2 . The lattice fringes of Bi_2O_3 and MoS_2 were taken and shown in Fig. 3b and c, which is assigned to the Bi_2O_3 (120) facet and MoS_2 (103) facet, respectively. Meanwhile, the independent lattice area of Bi_2S_3 (Fig. 3d) was captured when focused on the interface area between Bi_2O_3 and MoS_2 . In Fig. 3e, the different lattice fringe areas were distinguishably observed, which are ascribed to the Bi_2O_3 , Bi_2S_3 , and MoS_2 , respectively. The results demonstrate the successful formation of expected three-phase junction, $\text{Bi}_2\text{O}_3/\text{Bi}_2\text{S}_3/\text{MoS}_2$.

To confirm the chemical composition and investigate the surface valence state of these elements in $\text{Bi}_2\text{O}_3/\text{Bi}_2\text{S}_3/\text{MoS}_2$, the X-ray photoelectron spectroscopy (XPS) analysis has been performed, in which Bi, O, S, Mo elements can be observed (Fig. 4a). In the high resolution XPS spectrum of Bi 4f, as shown in Fig. 4b, two strong peaks appearing at 158.9 and 164.2 eV are ascribed to $\text{Bi} 4f_{7/2}$ and $\text{Bi} 4f_{5/2}$ of Bi^{3+} in the sample, respectively [11,32]. The peak at 162.1 and 163.2 eV can be assigned to $\text{S} 2p_{3/2}$ and $\text{S} 2p_{1/2}$ due to spin orbit separation of S element, which suggests the existence of S^{2-} in the final product [21,33]. In Fig. 4c, we can observe that the high resolution XPS spectrum of Mo 3d reveals two strong peaks at 229.1 and 232.4 eV corresponding to $\text{Mo} 3d_{5/2}$ and $\text{Mo} 3d_{3/2}$, respectively, which evidently demonstrates the valence state of molybdenum element is +4 in $\text{Bi}_2\text{O}_3/\text{Bi}_2\text{S}_3/\text{MoS}_2$ [34]. An apparent peak at 226.4 eV is ascribed to the binding energy of S 2s, which strongly indicates that the existence of MoS_2 . Furthermore, Fig. 4d shows the obvious peak at 529.5 eV, assigned to the Bi–O bonds in the sample of Bi_2O_3 , in good agreement with the previous results [35,36].

Raman spectroscopy as a useful tool at room temperature is usually used to distinguish the chemical bonds in the solid sample. In Fig. 5a, two apparent peaks at 323 and 457 cm^{-1} are ascribed to the vibration of Bi–O bond [37]. In the case of MoS_2 , the obvious peaks at 375 and 414 cm^{-1} in the inset picture are due to the typical E^{1g} and A_{1g} vibration modes, respectively. It is well-known that the E^{1g} vibration mode associates with in-layer displacements of Mo and S atoms while A_{1g} is related to out of layer symmetric displacements of S atoms along c axis [29]. For Bi_2S_3 prepared based on Bi_2O_3 microplates, the peaks at 964 and 429 cm^{-1} are assigned to nanostructured Bi_2S_3 vibration modes of Bi–S bonds [38]. When forming *p-n* heterojunction, the broad and weak vibration peaks at 391, 653, and 942 cm^{-1} are ascribed to Mo–S and Bi–S bonds, respectively, owing to the distortion of crystal structure at the interface. Besides, the peaks of Bi–O disappeared, which may be due to the coverage of Bi_2S_3 and MoS_2 . Combining the results of XPS and Raman, the interlayer Bi_2S_3 was formed between Bi_2O_3 and MoS_2 , which indicates that the three-component heterojunction was successfully constructed by a facile route.

The UV-vis absorption spectra of the samples are displayed in Fig. 5b. The absorption edge of Bi_2O_3 is about 500 nm, which to some degree exhibits photo response ability to the visible light. In the case of pure Bi_2S_3 and MoS_2 , broad absorption spectra were

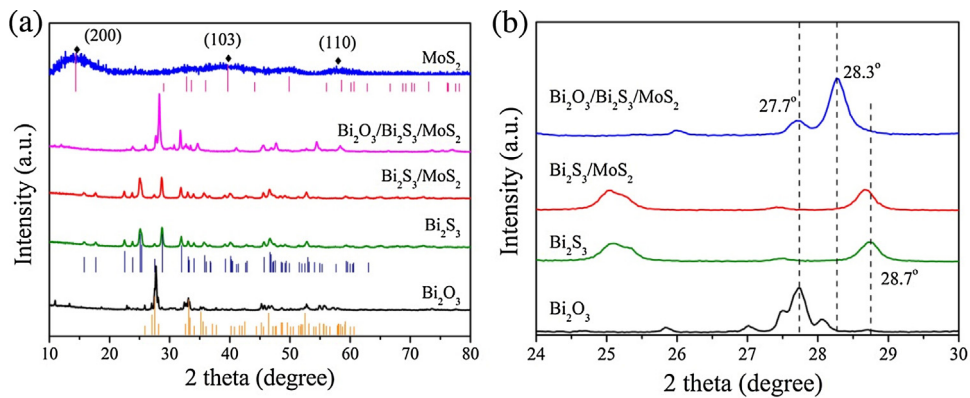


Fig. 1. The normal (a) and partially enlarged (b) XRD patterns of the samples prepared based on different nanostructures.

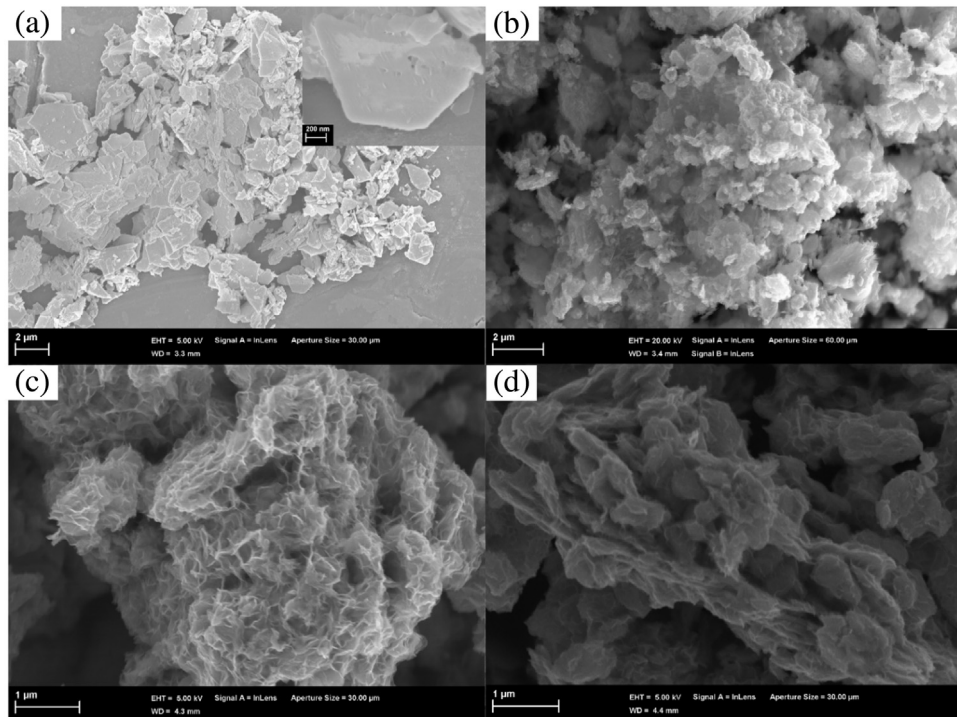


Fig. 2. SEM images of Bi₂O₃ (a), Bi₂S₃ (b), MoS₂ (c), Bi₂O₃/Bi₂S₃/MoS₂ (d).

observed, which indicates that they could absorb all photons at the whole range of UV and visible light. For the heterojunction systems, it is clearly seen that the absorption range of Bi₂O₃ was extended to the whole range of visible light as coupling Bi₂O₃ with Bi₂S₃ and MoS₂ for formation of *p-n* heterojunction. The corresponding band-gap energies are shown in Fig. 5c and d, estimated from the Tauc's equation, $(\alpha h) = A(\nu - E_g)^{n/2}$ [39]. In this equation, α , ν , A , and E_g are the absorption coefficient, light frequency, proportionality constant, and band gap, respectively. The value of n depends on the property of a semiconductor, where n values are 1 and 4 corresponding to direct and indirect band-gap semiconductors, respectively. The results present that the indirect band-gap energy of Bi₂O₃ moves from 2.48 to 0.81 eV, which evidently demonstrates the enhancement of photo-response ability for a heterojunction system.³⁵ In the case of pure Bi₂S₃ and MoS₂, the direct band gap energies were estimated to be 1.19 and 1.62 eV, respectively [40,41]. Corresponding to 1.2 eV of bulk MoS₂, the enlarged band gap of the as-obtained MoS₂ evidently indicates the formation of layered nanostructure due to the quantum confinement effect.

Meanwhile, the band gap energy of Bi₂S₃/MoS₂ was determined to be 1.30 eV, which suggests that the heterojunction still was formed between Bi₂S₃ and MoS₂.

The photoelectrochemical properties of these samples have been measured in order to investigate carriers transport behavior and efficiency at the nanojunction interface. As shown in Fig. 6a, electrochemical impedance spectroscopy (EIS) measurements were conducted and displayed in the manner of Nyquist diagram, in which the radius of each arc is related to the charge transfer process at the corresponding electrode-electrolyte interface. In general, a smaller radius of arc means a lower charge-transfer resistance [42]. It is observed that the pure Bi₂S₃ and MoS₂ exhibit smaller charge transfer resistance than Bi₂O₃, which indicates that Bi₂S₃ and MoS₂ possess excellent performance in the charge-transfer process. Therefore, once formation of Bi₂O₃/Bi₂S₃/MoS₂ heterojunction, the charge transfer resistance of Bi₂O₃ was reduced, which is beneficial to the transportation of the photoinduced charge carriers. In addition, the photocurrent response of the as-obtained samples as a working electrode

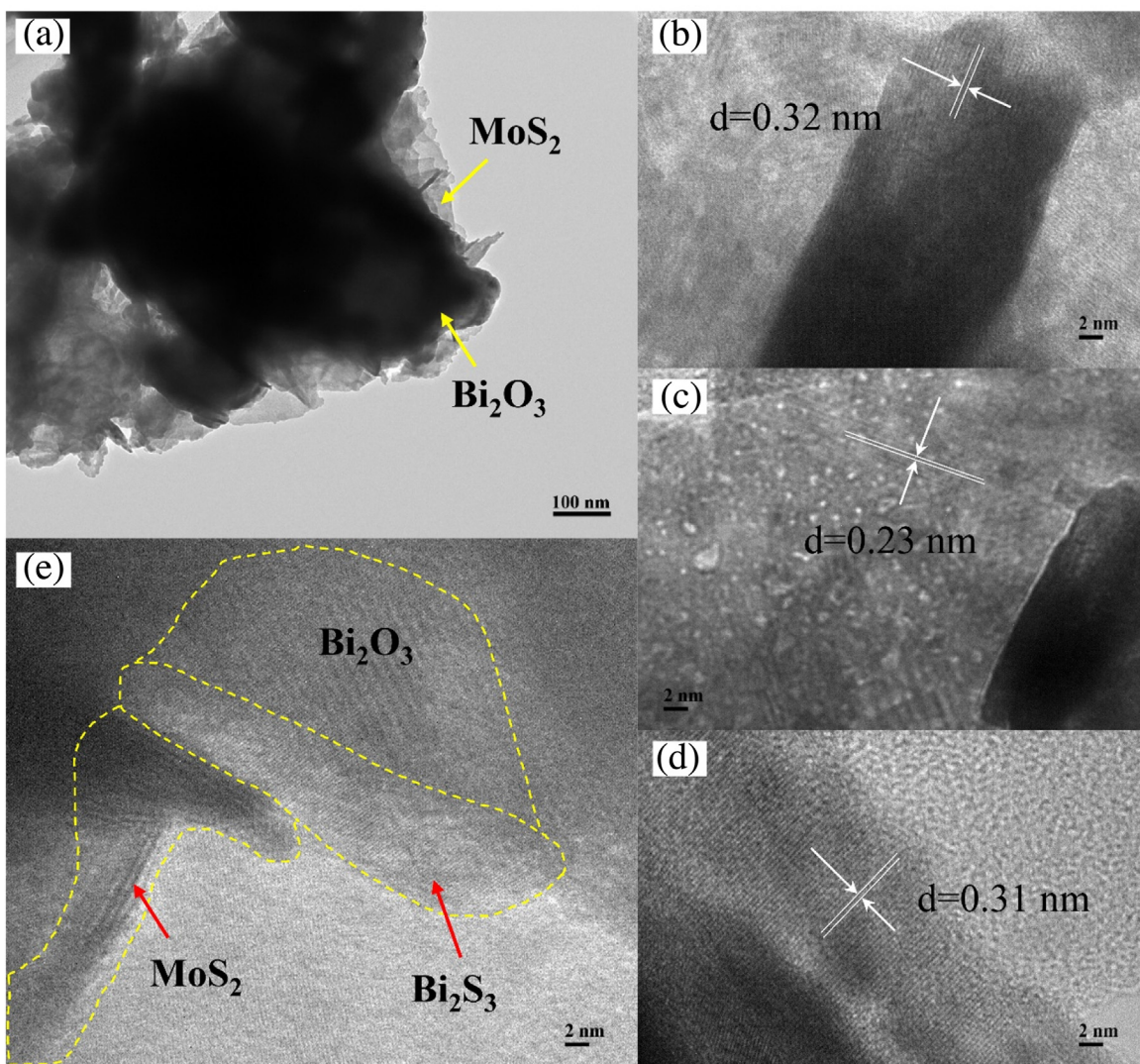


Fig. 3. Low magnification TEM image of $\text{Bi}_2\text{O}_3/\text{Bi}_2\text{S}_3/\text{MoS}_2$ (a), high magnification TEM images of Bi_2O_3 (b), MoS_2 (c), and Bi_2S_3 (d), high magnification TEM image of $\text{Bi}_2\text{O}_3/\text{Bi}_2\text{S}_3/\text{MoS}_2$ (e).

with light switch on and off were recorded and depicted in Fig. S2. Under the same condition, the photocurrent response of the three-component heterojunction system is about 6 and 2 times higher than that of the pure Bi_2O_3 and MoS_2 . The significant enhancement of photocurrent response originates from the photogenerated charge separation in $\text{Bi}_2\text{O}_3/\text{Bi}_2\text{S}_3/\text{MoS}_2$ heterojunction. It is worthy of note that the photocurrent density of $\text{Bi}_2\text{S}_3/\text{MoS}_2$ is less than that of $\text{Bi}_2\text{O}_3/\text{Bi}_2\text{S}_3/\text{MoS}_2$ heterojunction, which shows that the formation of the *n-p* heterojunction improves the electron-hole separation on the interface of the $\text{Bi}_2\text{O}_3/\text{Bi}_2\text{S}_3/\text{MoS}_2$ because of the different conduction band alignments and Fermi levels.

To further gain in-depth insights into the nature of the heterojunction, flat band potential and carrier concentrations were determined [43]. The detail of the Mott-Schottky (M-S) measurement has been described in experimental section. After that, the electrode potential versus saturated calomel electrode (SCE) were converting to reversible hydrogen electrode (RHE) potential according to the Nernst equation [44]

$$V_{\text{RHE}} = V_{\text{SCE}} + 0.059 \text{ pH} + V_{\text{SCE}}^0$$

Where V_{RHE} is the converted potential vs. RHE, $V_{\text{SCE}}^0 = 0.245 \text{ V}$ at pH 6.8, 25 °C, and V_{SCE} is the experimental potential measured against the $\text{Hg}/\text{Hg}_2\text{Cl}_2/\text{saturated KCl}$ reference electrode. The Mott-

Schottky (M-S) plots are shown in Fig. 6(b–f), in which the flat band potential at the electrode-electrolyte interface can be estimated by the following equation [45].

$$1/C^2 = (2/\varepsilon_r \varepsilon_0 e N_d A^2)[(V - V_{fb}) - kT/e]$$

Where C is the specific capacity, ε_r is the dielectric constant of the samples, ε_0 is the electric permittivity of vacuum ($8.85 \times 10^{-12} \text{ N}^{-1} \text{ C}^2 \text{ m}^{-2}$), N_d is the carrier density of the samples, A is the efficient area of electrode, V is the applied potential, V_{fb} is the flat band potential, k is the Boltzmann constant, T is the absolute temperature, and e is the electron charge ($1.602 \times 10^{-19} \text{ C}$). From Fig. 6b and d, we could observe a negative slope of the plots for MoS_2 and Bi_2S_3 , which confirms that both MoS_2 and Bi_2S_3 are *p*-type semiconductors. More interestingly, as shown in Fig. 6c, the positive slope of the plot suggests the *n*-type behavior of the Bi_2O_3 semiconductor, which is different from the previous reports. The flat band potentials of *p*-type MoS_2 , Bi_2S_3 , and *n*-type Bi_2O_3 , calculated from the x intercept of the liners region, are 0.82, 1.06, and -0.02 V vs. RHE, respectively. For $\text{Bi}_2\text{S}_3/\text{MoS}_2$, the negative slope of the M-S plot in Fig. 6e demonstrates that it is an expected *p*-type semiconductor with 0.73 V of flat potential. When they were coupled to each other to form a heterojunction, a *n-p* junction characteristic was observed in the M-S plot of $\text{Bi}_2\text{O}_3/\text{Bi}_2\text{S}_3/\text{MoS}_2$ where an inverted

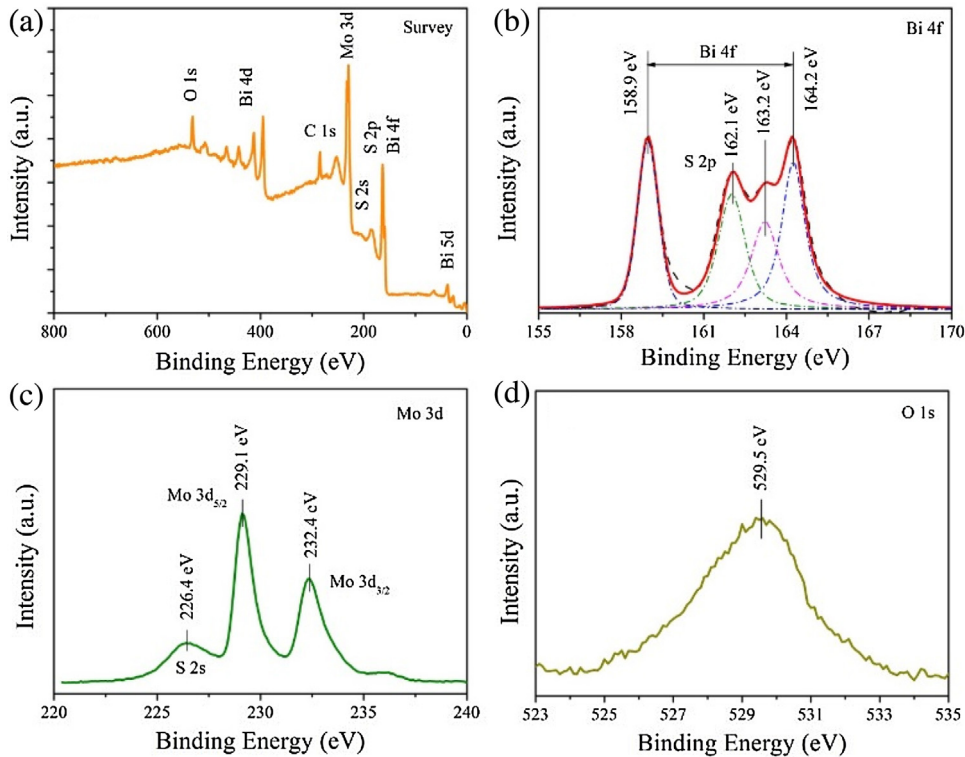


Fig. 4. XPS spectra of $\text{Bi}_2\text{O}_3/\text{Bi}_2\text{S}_3/\text{MoS}_2$, survey (a), Bi 4f and S 2p (b), Mo 3d (c) and O 1s (d).

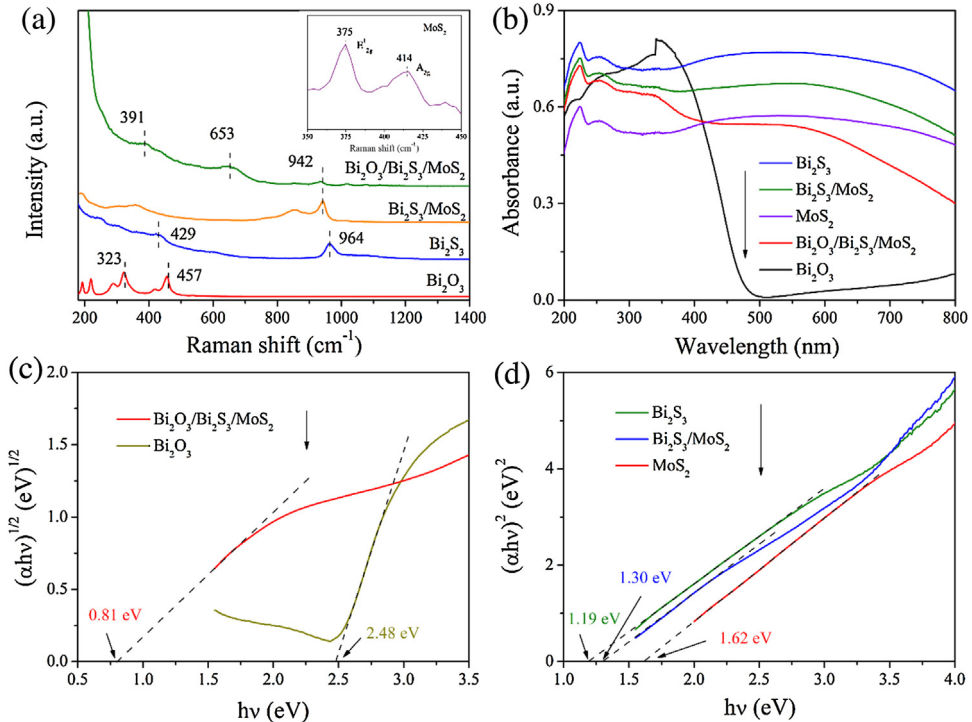


Fig. 5. (a) Raman spectra, (b) UV–vis absorption spectra, and (c, d) Tauc's plots of the as-prepared Bi_2O_3 , Bi_2S_3 , MoS_2 , $\text{Bi}_2\text{S}_3/\text{MoS}_2$, and $\text{Bi}_2\text{O}_3/\text{Bi}_2\text{S}_3/\text{MoS}_2$ heterojunctions. The inset picture is the Raman curve of pure MoS_2 .

"V-shape" was present (Fig. 6f). This indicates that two different (*n*- and *p*-type) electronic behaviors are exhibited by the electrode [18]. Furthermore, the density of charge carriers was obtained from the slope of M-S plot, according to the equation

$$N_d = \left(2/\epsilon_r \epsilon_0 e A^2\right) [d(1/C^2)/dV]^{-1}$$

Consequently, the donor densities of *p*-type MoS_2 , Bi_2S_3 , and *n*-type Bi_2O_3 were equal to 3.49×10^{14} , 1.68×10^{15} , and $2.61 \times 10^{13} \text{ cm}^{-3}$ in the dark, respectively, while the donor densities of $\text{Bi}_2\text{S}_3/\text{MoS}_2$ and $\text{Bi}_2\text{O}_3/\text{Bi}_2\text{S}_3/\text{MoS}_2$ were measured to be 7.45×10^{14} and $5.65 \times 10^{13} \text{ cm}^{-3}$ in the dark, respectively. The

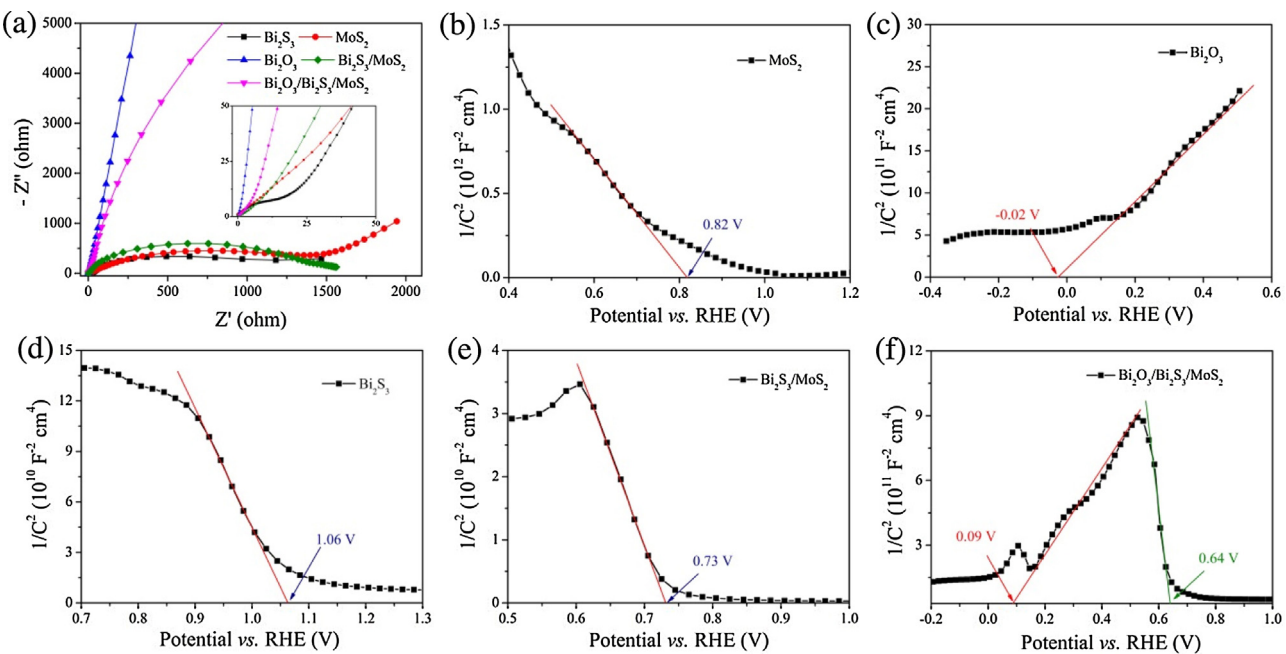


Fig. 6. Nyquist plot of electrochemical impedance spectroscopy (a), the inset image is partial magnificence of the Nyquist plot; Mott-Schottky curves of MoS₂ (b), Bi₂O₃ (c), Bi₂S₃ (d), Bi₂S₃/MoS₂ (e), and Bi₂O₃/Bi₂S₃/MoS₂ (f).

increased charge carrier densities in the *n*-Bi₂O₃/*p*-Bi₂S₃/*p*-MoS₂ heterojunction system indicated that the formation of nanoscaled *n-p* junction could efficiently create a sufficient space charge layer to enhance the charge carrier transportation.

Apart from their unique photophysical and electrochemical properties, the three-phase heterojunction system is also expected to possess photocatalytic activity toward water oxidation, as widely reported in the literature. Fig. 7a presents the photocatalytic activities of the as-obtained samples evaluated by oxidation of water molecules. The Bi₂O₃/Bi₂S₃/MoS₂ exhibited an apparent photocatalytic activity with 61 μmol/L of O₂ evolution in 3 h under simulated solar light irradiation. In contrast, pure Bi₂S₃ and MoS₂ showed weak photocatalytic performance for water oxidation, which is agreement with the previous reports due to the high position of valence band leading to insufficient oxidation ability, whereas the pure Bi₂O₃ gave a considerable photocatalytic activity with 47 μmol/L of O₂ evolution. Introducing of MoS₂ to form the *p-n* heterojunction, the ability of O₂ evolution was remarkably enhanced, and the initial O₂ evolution rate of the Bi₂O₃/Bi₂S₃/MoS₂ at 529.1 μmol h⁻¹ g⁻¹ cat is 1.5 times than that of the pure Bi₂O₃, 355.8 μmol h⁻¹ g⁻¹ cat in Fig. 7b. These results demonstrate that the formation of *p-n* junction improves the transfer efficiency of charge carriers and simultaneously suppresses the recombination rate of photogenerated electron-hole pairs. In addition, owing to the technical difficulty in preparing pure Bi₂O₃/MoS₂ under the above-mentioned hydrothermal condition, we mechanically mixed Bi₂O₃ with MoS₂ for testing the water oxidation performance. The mixed Bi₂O₃/MoS₂ exhibited the slightly less activity in water oxidation performance than the pure Bi₂O₃, which indicates that no effective heterojunction was formed between Bi₂O₃ and MoS₂ through mechanically mixing way. Meanwhile, the improvement of photocatalytic activity of Bi₂S₃/MoS₂ was observed by comparison with the pure Bi₂S₃ and MoS₂, which suggests the heterojunction formation between Bi₂S₃ and MoS₂ can also lead to the increase of charge separation efficiency.

To further clearly verify the photocatalytic performance, the specific surface areas of all the samples were investigated, as shown in Table S1. It was observed that the specific surface areas of Bi₂O₃,

Bi₂S₃/MoS₂, and Bi₂O₃/Bi₂S₃/MoS₂, are similar, which could rule out the specific surface area as an obvious factor to induce the difference in catalytic activity. The stability of photocatalytic performance of the heterojunction system was also investigated, as shown in

Fig. S3. It is clearly displayed that the yield of oxygen decreased to 60% by comparison with the fresh catalyst when the three-component catalyst was recycled three times, which results from the reductive deposition of silver ions on the surface of the catalyst and thus hinders the photon absorption.

Furthermore, to analyze the utilization efficiency of holes without Ag⁺ as an electron scavenger, the organic dye (methyl blue, MB) was used as a target pollutant, as shown in Fig. S4. It is observed that the Bi₂O₃/Bi₂S₃/MoS₂ system exhibits the best photocatalytic degradation efficiency, 90%, in 6 h under simulated solar light irradiation. The reactive oxygen species (ROS) have been proved by using EPR tool, where both of hydroxyl (·OH) and superoxide radicals (O₂^{·-}) were detected in Fig. S5 and demonstrated that the heterojunction system could produce the effective ROS to damage pollutants. More interesting, the pure Bi₂O₃ presented a weak photocatalytic activity for degradation of MB, which is consistent with the previous reports [10]. We speculate that the photocatalytic ability of the pure Bi₂O₃ in water splitting process mainly originates from the high energetic holes upon the introduction of Ag⁺ as an electron scavenger, which improves the separation efficiency of photogenerated electron-hole pairs and thus enhances the production of gaseous oxygen. Combining the results, it is confirmed that the photocatalytic performance of pure Bi₂O₃ is highly enhanced after the formation of the three-phase *p-n* heterojunction in the Bi₂O₃/Bi₂S₃/MoS₂ sample.

On the basis of photophysical and electrochemical characterizations, band assignment of the samples is displayed in Fig. 8a. Commonly, for *n*-type Bi₂O₃, the Fermi level is close to the conduction band, whereas for *p*-type Bi₂S₃ and MoS₂, the Fermi level approaches to the valence band. When the *n*-type Bi₂O₃ was coupled with the *p*-type Bi₂S₃ and MoS₂, *p-n* heterojunctions among these semiconductors were formed, resulting in the realignment of their valence and conduction bands due to the thermal equilib-

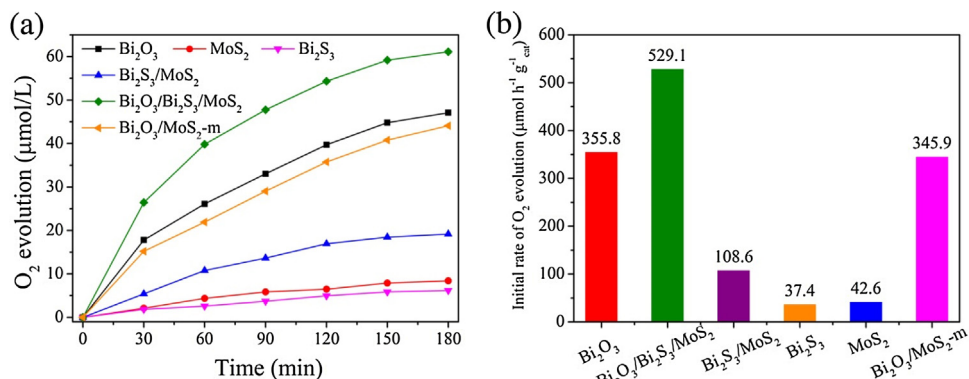


Fig. 7. Photocatalytic activity for O_2 evolution (a), initial water oxidation rate (b) of the different samples under simulated solar light irradiation. The experimental condition: catalyst, 0.5 g/L; concentration of AgNO_3 , 0.03 M; La_2O_3 , 0.2 g; volume, 200 mL; temperature, 25 °C.

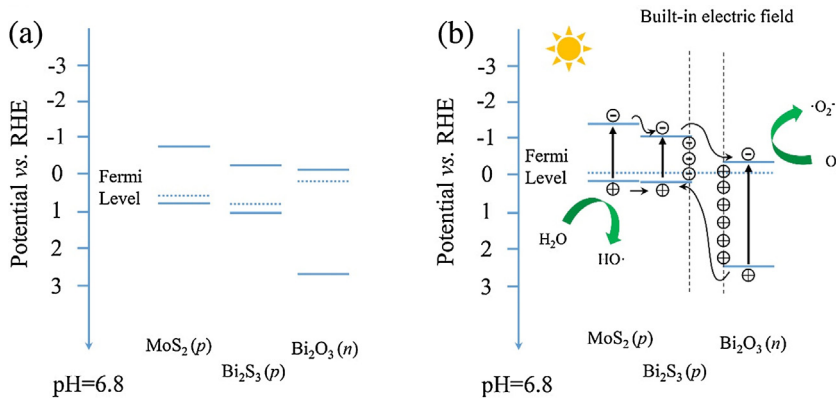


Fig. 8. Schematic diagram for (a) energy band of Bi_2O_3 , MoS_2 , and Bi_2S_3 and (b) the formation of the three-phase p - n heterojunction and the possible charge separation.

rium of different Fermi levels and the formation of built-in electric field [46,47]. This allows the energy bands of Bi_2O_3 and Bi_2S_3 , MoS_2 shift downward and upward, respectively, along the Fermi level, as shown in Fig. 8b. When the $\text{Bi}_2\text{O}_3/\text{Bi}_2\text{S}_3/\text{MoS}_2$ heterojunction system was irradiated by visible light, Bi_2S_3 and MoS_2 with a narrow band gap are excited to produce electrons and holes. The photoinduced electrons on the conduction band of the p -type Bi_2S_3 and MoS_2 transfer to that of n -type Bi_2O_3 , whereas the holes remain in the valence band of the Bi_2S_3 and MoS_2 . As discussed above, the p - n heterojunction realize suppression of the recombination of photoinduced electron-hole pairs, which allows more photogenerated electrons and holes to participate in the reduction and oxidation reactions for oxidizing water molecules and pollutants.

4. Conclusions

In summary, a novel p - n heterojunction system has been fabricated for the first time through a facile and practical hydrothermal method. After synthesis of Bi_2O_3 microplates, Bi_2S_3 phase was formed by coupling Bi_2O_3 with MoS_2 , resulting in the production of three-component heterojunction. The as-obtained $\text{Bi}_2\text{O}_3/\text{Bi}_2\text{S}_3/\text{MoS}_2$ n - p heterojunction exhibits a higher photocatalytic water oxidation than pure Bi_2O_3 and Bi_2S_3 under simulated solar light irradiation. The initial rate of the three-component heterojunction for O_2 evolution is 1.5 and 12.4 times higher than that of pure Bi_2O_3 and MoS_2 , respectively. In addition, the photoelectrochemical results show the enhanced transportation feature and increased donor density after the formation of the n - p heterojunction, which exerts a positive impact on improving the harvesting efficiency of solar energy and reducing the transportation barrier

of charge carrier inside the n - p heterojunction system. The mechanism of the enhanced photocatalytic performance is ascribed to the combination of Bi_2O_3 and MoS_2 extending light absorption and the formation of the n - p heterojunction with better energy band matching between Bi_2O_3 and Bi_2S_3 , MoS_2 . This study provides a new design and preparation of other high performance p - n heterojunction nanomaterials for photocatalytic applications, such as hydrogen and oxygen production, CO_2 reduction, and solar harvesting.

Acknowledgements

This work was supported financially by Australian Research Council (DP150103026), the National Natural Science Foundation of China (21507029, 21501138), the Natural Science Foundation of Hubei Province (2015CFB177). The authors also acknowledge the use of equipment, scientific and technical assistance of the WA X-Ray Surface Analysis Facility, funded by the Australian Research Council LIEF grant LE120100026.

Appendix A. Supplementary data

Supplementary data associated with this article can be found, in the online version, at <http://dx.doi.org/10.1016/j.apcatb.2016.06.071>.

References

- [1] X. Chen, S. Shen, L. Guo, S.S. Mao, Chem. Rev. 110 (2010) 6503–6570.
- [2] Z. Zou, J. Ye, K. Sayama, H. Arakawa, Nature 414 (2001) 625–627.

[3] G. Liu, J. Hall, N. Nasiri, T. Gengenbach, L. Spiccia, M. Cheah, A. Tricoli, *ChemSusChem* 8 (2015) 4162–4171.

[4] A. Frame, T. Townsend, R. Chamousis, E. Sabio, T. Dittrich, N. Browning, F. Osterloh, *J. Am. Chem. Soc.* 133 (2011) 7264–7267.

[5] Y. Zhang, E. Judkins, D. MicMillin, D. Mehta, T. Ren, *ACS Catal.* 3 (2013) 2474–2478.

[6] R. Matheu, L. Francas, P. Chernev, M. Ertem, V. Batista, M. Haumann, X. Sala, A. Llobet, *ACS Catal.* 5 (2015) 3422–3429.

[7] X. Deng, H. Bongard, C. Chan, H. Tuysuz, *ChemSusChem* 9 (2016) 409–415.

[8] F. Meng, J. Li, S. Cushing, J. Bright, M. Zhi, J. Rowley, Z. Hong, A. Manivannan, A. Bristow, N. Wu, *ACS Catal.* 3 (2013) 746–751.

[9] G. Zhang, S. Zang, Z. Lan, C. Huang, G. Li, X. Wang, *J. Mater. Chem. A* 3 (2015) 17946–17950.

[10] M. Muruganandham, R. Amutha, G. Lee, S. Hsieh, J. Wu, M. Sillanpaa, *J. Phys. Chem. C* 116 (2012) 12906–12915.

[11] W. Sun, H. Zhang, J. Lin, *J. Phys. Chem. C* 118 (2014) 17626–17632.

[12] C. Lee, S. Jeong, N. Myung, K. Rajeshwar, *J. Electrochem. Soc.* 161 (2014) 499–503.

[13] S. Park, S. Kim, G.J. Sun, C. Lee, *ACS Appl. Mater. Interfaces* 7 (2015) 8138–8146.

[14] T. Xie, C. Liu, L. Xu, J. Yang, W. Zhou, *J. Phys. Chem. C* 117 (2013) 24601–24610.

[15] C.F. Lai, C.C. Chang, M.H. Wen, C.K. Lin, M.K. Wu, *Phys. Status Solidi A* 210 (2013) 1133–1136.

[16] H. Li, Y. Zhou, W. Tu, J. Ye, Z. Zou, *Adv. Funct. Mater.* 25 (2015) 998–1013.

[17] H. Wang, L. Zhang, Z. Chen, J. Hu, S. Li, Z. Wang, J. Liu, X. Wang, *Chem. Soc. Rev.* 43 (2014) 5234–5244.

[18] F. Meng, J. Li, S.K. Cushing, M. Zhi, N. Wu, *J. Am. Chem. Soc.* 135 (2013) 10286–10289.

[19] M. Wang, L. Sun, Z. Lin, J. Cai, K. Xie, C. Lin, *Energy Environ. Sci.* 6 (2013) 1211–1220.

[20] X. Zong, H.J. Yan, G.P. Wu, G.J. Ma, F.Y. Wen, L. Wang, C. Li, *J. Am. Chem. Soc.* 130 (2008) 7176–7177.

[21] B. Weng, X. Zhang, N. Zhang, Z.R. Tang, Y.J. Xu, *Langmuir* 31 (2015) 4314–4322.

[22] H. Li, K. Yu, X. Lei, B. Guo, C. Li, H. Fu, Z. Zhu, *Dalton Trans.* 44 (2015) 10438–10447.

[23] K. Duan, Y. Du, Q. Feng, X. Ye, H. Xie, M. Xue, C. Wang, *ChemCatChem* 6 (2014) 1873–1876.

[24] Z. Lu, H. Zhang, W. Zhu, X. Yu, Y. Kuang, Z. Chang, X. Lei, X. Sun, *Chem. Commun.* 49 (2013) 7516–7518.

[25] B. Zhu, B. Lin, Y. Zhou, P. Sun, Q. Yao, Y. Chen, B. Gao, *J. Mater. Chem. A* 2 (2014) 3819–3827.

[26] M. Shen, Z. Yan, L. Yang, P. Du, J. Zhang, B. Xiang, *Chem. Commun.* 50 (2014) 15447–15449.

[27] T. Saison, N. Chemin, C. Chanefiac, O. Durupthy, V.R. Ruaux, L. Mariey, F.O. Maugeï, P. Beaunier, J.P. Jolivet, *J. Phys. Chem. C* 115 (2011) 5657–5666.

[28] L. Ma, Q. Zhao, Q. Zhang, M. Ding, J. Huang, X. Liu, Y. Liu, X. Wu, X. Xu, *RSC Adv.* 4 (2014) 41636–41641.

[29] Z. Wu, C. Tang, P. Zhou, Z. Liu, Y. Xu, D. Wang, B. Fang, *J. Mater. Chem. A* 3 (2015) 13050–13056.

[30] B. Lei, G.R. Li, X.P. Gao, *J. Mater. Chem. A* 2 (2014) 3919–3925.

[31] Z. Zhang, W. Wang, L. Wang, S. Sun, *ACS Appl. Mater. Interfaces* 4 (2012) 593–597.

[32] F. Dong, X. Feng, Y. Zhang, C. Gao, Z. Wu, *RSC Adv.* 5 (2015) 11714–11723.

[33] C. Liu, L. Wang, Y. Tang, S. Luo, Y. Liu, S. Zhang, Y. Zeng, Y. Xu, *Appl. Catal. B: Environ.* 164 (2015) 1–9.

[34] S.N. Guo, Y.L. Min, J.C. Fan, Q.J. Xu, *ACS Appl. Mater. Interfaces* 8 (2016) 2928–2934.

[35] H.Y. Jiang, P. Li, G. Liu, J. Ye, J. Lin, *J. Mater. Chem. A* 3 (2015) 5119–5125.

[36] M. Ge, C. Cao, S. Li, S. Zhang, S. Deng, J. Huang, Q. Li, K. Zhang, S.S. Al-Deyab, Y. Lai, *Nanoscale* 7 (2015) 11552–11560.

[37] J. In, I. Yoon, K. Seo, J. Park, J. Choo, Y. Lee, B. Kim, *Chem. Eur. J.* 17 (2011) 1304–1309.

[38] J. Ota, S.K. Srivastava, *J. Phys. Chem. C* 111 (2007) 12260–12264.

[39] A. Zhu, Q. Zhao, X. Li, Y. Shi, *ACS Appl. Mater. Interfaces* 6 (2014) 671–679.

[40] I. Zumeta-Dubé, J.L. Ortiz-Quiñonez, D. Díaz, C. Trallero-Giner, V.F. Ruiz-Ruiz, *J. Phys. Chem. C* 118 (2014) 30244–30252.

[41] X. Ren, L. Pang, Y. Zhang, X. Ren, H. Fan, S. Liu, *J. Mater. Chem. A* 3 (2015) 10693–10697.

[42] X. Wang, J. Xie, C.M. Li, *J. Mater. Chem. A* 3 (2015) 1235–1242.

[43] M.H. Jung, M.G. Kang, *J. Mater. Chem.* 21 (2011) 2694–2700.

[44] M. Li, L. Zhang, X. Fan, Y. Zhou, M. Wu, J. Shi, *J. Mater. Chem. A* 3 (2015) 5189–5196.

[45] A.A. Dubale, W.N. Su, A.G. Tamirat, C.J. Pan, B.A. Aragaw, H.M. Chen, C.H. Chen, B.J. Hwang, *J. Mater. Chem. A* 2 (2014) 18383–18397.

[46] J. Sun, X. Li, Q. Zhao, J. Ke, D. Zhang, *J. Phys. Chem. C* 118 (2014) 10113–10121.

[47] Y. Peng, M. Yan, Q.G. Chen, C.M. Fan, H.Y. Zhou, A.W. Xu, *J. Mater. Chem. A* 2 (2014) 8517–8524.